

Case History

Caprock integrity at Çanakkale-Tuzla hydrothermal system inferred from magnetotelluric modeling using particle swarm optimization

Ersin Büyük¹ and Abdullah Karaman²

ABSTRACT

The impermeable caprock within a geothermal system serves the purpose of effectively sealing the reservoir, resulting in an elevation of both pressure and temperature. This sealing mechanism plays a crucial role in the long-term preservation of the system while also contributing to its overall sustainability. Caprock failure subsequent to seismic activity near a geothermal site can lead to the permeation of the caprock structure, resulting in diminished sealing capabilities and a decline in the reservoir temperature. In addition, this process alters the geochemical composition of the water by creating a hydrothermal mixture zone that disrupts the resistivity structure of the caprock, which is typically characterized by low resistivity values due to its substantial clay content and mineral alteration. This study focuses on investigating the integrity of the caprock at the Çanakkale-Tuzla

geothermal field in Turkey, where water temperature and conductivity were reported to have decreased after a moderate-magnitude earthquake and subsequent aftershocks. For this purpose, we have performed magnetotelluric (MT) measurements, a method known for its sensitivity to geochemical reactions. These measurements are conducted along two parallel profiles that encompassed a total of 32 stations. The particle swarm optimization (PSO) technique is used to overcome the subtle difficulties associated with conventional inversion methods in modeling the MT data of complex formations. This is the first study that overcomes the difficulties emanating from the caprock failure by modeling MT data using PSO. Our modeling approach produces resistivity images that we interpreted as the signature of the failed caprock following the earthquake at the study site. Our results appear to confirm the documented geochemical changes, or hydrothermal mixture zone around the caprock structure.

INTRODUCTION

The caprock, which acts as a critical component of a geothermal system by sealing the reservoir and maintaining pressure, is susceptible to damage from nearby earthquakes (Yamaya et al., 2013), volcanic activity induced by seismicity (Iguchi, 2013), and pore-pressure changes induced by magma intrusion (Mannen et al., 2021). In a typical reservoir, the presence of an impermeable caprock serves to inhibit any potential leakage and effectively seals the reservoir, facilitating the accumulation of high temperature and pressure conditions that enhance well productivity. The caprock's integrity, characterized by these attributes, guarantees the sustain-

able exploitation of the reservoir, in contrast to caprock with limited sealing capacity, which results in leakage (Song and Zhang, 2013; Maffucci et al., 2016). Therefore, methods of inspecting the geometry and integrity of a caprock are valuable for postearthquake assessments to maintain sustainable exploitation of a geothermal reservoir.

A caprock structure is usually characterized by mineral alteration leading to a high clay content, resulting in a structure identified clearly with a low electrical resistivity (Muñoz, 2014) and low permeability (Jones and Dumas, 1993; Ussher et al., 2000; Samrock et al., 2015; Lichoro et al., 2017). However, the task of distinguishing caprock failure by using magnetotelluric (MT) measurements

Manuscript received by the Editor 29 March 2023; revised manuscript received 10 November 2023; published ahead of production 23 November 2023; published online 30 January 2024.

¹Gümüşhane University, Department of Geophysical Engineering, Gümüşhane, Turkey and TUBİTAK, Marmara Research Center, Earth Sciences Research Group, Kocaeli, Turkey. E-mail: ebuyuk@gumushane.edu.tr (corresponding author).

²Istanbul Technical University, Department of Geophysical Engineering, Istanbul, Turkey. E-mail: karaman@itu.edu.tr.

© 2024 Society of Exploration Geophysicists. All rights reserved.

inverted with traditional inversion techniques can pose challenges due to the structural intricacies arising from the nonsealing characteristics of the caprock. This is because the dependence on the initial model required for conventional inversion methods usually results in a final model that is trapped around a local minimum because of too large absolute gradient of an objective function explicitly evaluated by a numerical method (Shaw and Srivastava, 2007; Yuan et al., 2009; Fernández Martínez et al., 2010; Pekşen et al., 2014; Pallerio et al., 2015; Godio and Santilano, 2018). Moreover, partial derivatives in a nonlinear mathematical model can lead to a singularity in the basic model equation system with conventional inversion methods. Clearly, solving a singular system requires tedious approximation methods, such as phasing out the zero eigenvalues and vectors and replacing zero or small eigenvalues with slightly greater values, which is equivalent to adding noise to the system. Similar discussions can be found in Bonabeau et al. (1999) and Kennedy and Eberhart (2002).

Şanlıyüksel Yücel et al. (2021) monitor a decrease in the temperature and electrical conductivity of geothermal water close to the Çanakkale-Tuzla geothermal field after the Mw = 5.3 earthquake on 6 January 2017 and the subsequent aftershocks until 26 March 2017. We consider that these observations are highly related to the postearthquake activity resulting in the failure of the caprock integrity in the field. Unfortunately, we have no evidence that the caprock provided a seal prior to the earthquake. The determination of caprock integrity following the earthquake was conducted in this study using the MT data acquired within the geothermal field, as shown in Figure 1. In addition, we used particle swarm optimization (PSO) as a viable alternative to traditional inversion methods in the context of one-dimensional modeling of the MT data set. This dimensional modeling offers enhanced resolution in detecting caprock structure compared to two- or three-dimensional modeling, as indicated by Cumming and Mackie (2010). PSO as a modern global optimization method has been applied to MT and other types of electromagnetic data to overcome the subtle difficulties encountered in conventional inversion techniques. For example, Godio and Santilano (2018) use PSO for regularized 1D inversion of MT data, Cui et al. (2020) invert MT data combining PSO and regularized least-squares, and Pace et al. (2019) implement PSO for 2D modeling. Moreover, Shaw and Srivastava (2007) study the applicability of PSO for 1D modeling of induced polarization and MT data, Karcioğlu and Gürer (2019) implement PSO to obtain a smooth model from radio MT data, Li et al. (2019) use PSO to model a mine roadway from transient electromagnetic data, Olalekan and Di (2017) use PSO for groundwater exploration from time-domain electromagnetic data, and Kaplanvural et al. (2020) apply it to invert ground-penetrating radar data to delineate different types of plastic pipes. Pace et al. (2021) have also published a recent review indicating the growing body of literature on PSO. Although the implementation of the PSO algorithm requires high computational costs, a number of studies such as Eberhart and Shi (1998), Kennedy and Spears (1998), Hassan et al. (2005), Gill et al. (2006), Yuan et al. (2009), and Büyük et al. (2017) have highlighted the rapid convergence properties of PSO compared with genetic algorithms or simulated annealing. The efficacy of our modeling approach in ascertaining the caprock geometry was evident, thus reinforcing our confidence in the robustness of PSO as a modeling technique for the MT data acquired on a geothermal field. In this study, to the best of the authors' knowledge, PSO was used for the first time to obtain a 1D geoelectric resistivity cross section of a reservoir using MT data sets acquired soon after an earthquake, which usually causes a slight drop in temperature and alters the geochemistry of the geothermal field, as observed by Şanlıyüksel Yücel et al. (2021).

SITE DESCRIPTION

General geology

The Biga Peninsula is the study site located between Ezine and Ayvacık districts, at Çanakkale province of Turkey, and is bounded by Edremit Bay to the south and the Aegean Sea to the west, as shown in Figure 1. The Biga Peninsula, affected by the closure of the Neo-Tethys Ocean in the Late Cretaceous, has a very complex structure resulted from series of tectonic and magmatic processes during the period that began with the closure of the oceanic crust and ended with the extensional process in the Early Miocene-Pliocene

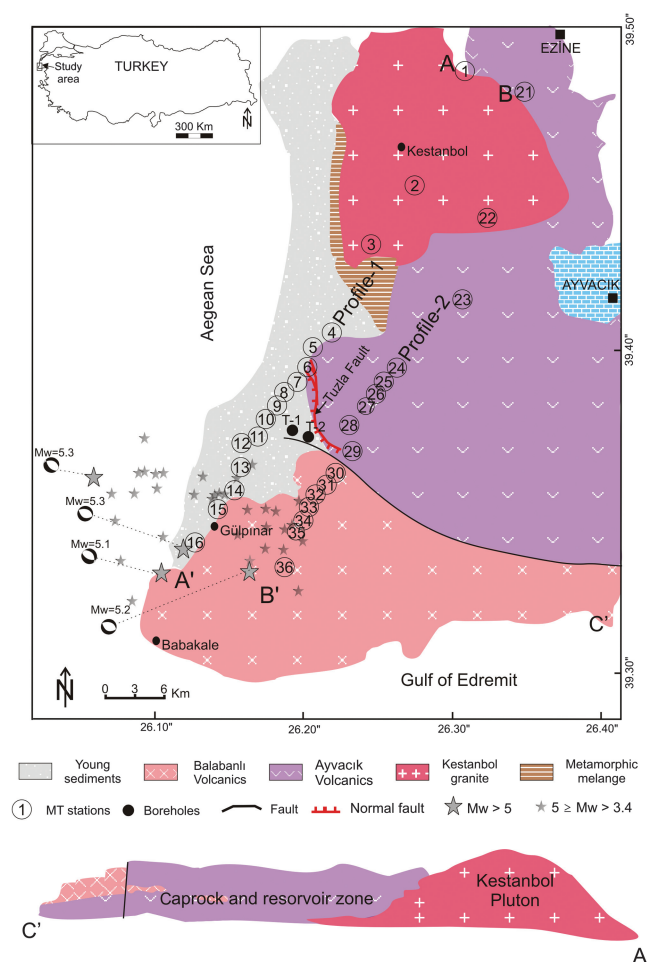


Figure 1. (a) The MT measurement stations and Profiles 1 and 2, earthquake epicenters along with moment tensor solutions (Özden et al., 2018), boreholes T-1 and T-2 over base geology map reconstructed from Karacık and Yılmaz (1998) and Akal (2013), and MTA active fault map (Emre and Doğan, 2010); (b) extension of caprock and reservoir zone along A-C' profile (modified from Karacık and Yılmaz, 1998). The fault along the east-west direction (dark solid line) is a speculative fault; thus, it was described as "unspecified fault" in the cited reference.

(McKenzie, 1978; Dewey and Şengör, 1979; Beccaleto, 2003). The igneous rocks were formed by the crust-mantle interaction caused by the northward movement of the Neo-Tethys oceanic, which subducted under the Sakarya continent. Following the complete closure, a continental collision in the Paleocene-Eocene and subsequent north-south compression led to partial melting of the lithospheric mantle that initiated the magmatic process in the Eocene-Oligocene-Miocene (Yılmaz, 1990; Okay et al., 1996; Aldanmaz et al., 2000; Altunkaynak and Genç, 2008). The Kestanol plutons and Ayvacık volcanics, shown in Figure 1, were formed during this compression process (Yılmaz et al., 2001). From the Early Miocene to the Late Pliocene, the north-south compressional regime was replaced with a north-south extensional regime that initiated the volcanic activities related to fragmentation and thinning of the lithospheric and asthenospheric uplift (Yılmaz et al., 2001; Aslan et al., 2017). Asthenospheric uplift within an extensional regime and increased geothermal gradient also led to partial melting in the Early Miocene. During this period, northeast-southwest horsts, Miocene grabens, and sedimentation occurred, but the topographic features of graben-horst structures were eroded by various phases and lacustrine sediments (Karacık and Yılmaz, 1998; Altunkaynak et al., 2012; Aslan et al., 2017).

The Biga Peninsula, rich in industrial raw materials, metallic minerals, and hydrothermal resources, exhibits complex structural features of tectonic and magmatic origin that have received much attention in several studies (e.g., McKenzie, 1978; Dewey and Şengör, 1979; Taymaz et al., 1991; Okay et al., 1996; Karacık and Yılmaz, 1998; Yılmaz et al., 2001; Altunkaynak et al., 2012). Karacık and Yılmaz (1998), as illustrated in Figure 1, describe that the site hosts a combination of Sakarya continental and oceanic crustal units corresponding to a metamorphic basement, plutonic intrusions, volcanic rocks, and sedimentary units. Fytikas et al. (1976) and Yılmaz et al. (2001) indicate that magmatic processes and magmatism began with the intrusion of the Kestanol granitic pluton into the metamorphic basement during the Late Oligocene and Early Miocene period. Based on their structural features, Karacık and Yılmaz (1998) name the volcanic rocks at this site the Ayvacık Volcanics (Late Cretaceous to Middle Miocene) in the north of the Tuzla Fault (Figure 1) with their bedded features and Balabanlı Volcanics (Early Miocene) in the south complicated by several dikes whose effects can be observed at the surface (Fytikas et al., 1976; Altunkaynak and Genç, 2008). The logs of two production wells (Akkuş et al., 2005, pp. 97–103), labeled as T-1 and T-2 that are screened at depths of 814 and 1020 m, respectively, (see Figure 2), indicate volcanic rocks such as andesite-dacite lavas, tuffs, and ignimbrites point out the hydrothermal zone. The production rate of the wells and the reservoir temperature of the geothermal water were measured as 130 tons/hour and approximately 170°C, respectively (Akkuş et al., 2005; Baba et al., 2015).

Pre- and postearthquake water chemistry

The principal geologic feature in the studied area is the Tuzla Fault, which exhibits a normal component and a dip angle of approximately 70° toward the south-southwest direction. This fault plays a crucial role in facilitating the formation of conduits necessary for the development of a hydrothermal system. After the main shock of Mw = 5.3 on 6 February 2017 at 03:51 (UTM), the Network of the Kandilli Observatory and Earthquake Research Institute recorded more than 4000 earthquakes from 14 January to 26 March

2017. The seismic events shown in Figure 1, which had moment magnitudes (Mw) ranging from 3.4 to 5, suggest that most of the focal mechanisms observed are consistent with a stress state characterized by normal to oblique faulting (Özden et al., 2018).

Şanlıyüksel Yücel et al. (2021) monitor the temporal variations of temperature and chemical composition of geothermal water after the Mw = 5.0 earthquake in the Kestanol geothermal fields, which are located approximately 15 km north of the Tuzla field. Although the time interval for sampling before and after the earthquake was on the order of a few months, a pre- and postearthquake temperature drop of approximately 0.7°C, water conductivity drop of approximately 900 µS/cm, and also a noticeable change in water chemistry were reported as a direct effect of the earthquakes. The observed postearthquake alterations can be attributed to changes in pore pressure and the introduction of cold water from aquifers above, leading to mechanical mixing and dilution of chemical composition. Unfortunately, the reported water chemistry data set does not contain densely sampled observations pertaining to the pre- and postearthquake variations that can be attributed to the immediate response of the geothermal field prior to the attainment of thermal and/or chemical equilibrium.

However, the abundant illite and mixed layers of illite-smectite clay minerals reported by Bozkaya et al. (2016) at the site are mostly related to hydrothermal fluids associated with the stress regime that occurred on the Biga Peninsula. Nevertheless, their field observations about lacking complete transition in such mixed layers from smectite to illite may be interpreted as an indication of moderate temperature conditions. The prevalence of smectite and illite clay minerals may be considered as an indication of fluctuations in fluid temperature that can be interpreted as failed caprock after a series of seismic events. Isotopic and chemical analyzes of surface water by Yalçın (1989) and Mutzenberg (1997) indicate that geothermal water mixed with seawater was approximately 70% associated with fossil metamorphism. Şener and Gevrek (2000) and Baba et al. (2015) report the origin of the salinity of the geothermal water as seawater because the mineral composition of the surrounding rocks does not provide a favorable environment.

FIELD DATA

Profile design

Figure 1 shows the 32 unevenly spaced stations for MT measurements along two profiles across the Tuzla Fault. The grid spacing was reduced near the geothermal field from the center to the southern end of the profiles to optimize the field work load. The decision was made to align the profiles parallel to the shoreline to mitigate the impact of conductive seawater. However, the distance of the profiles from the shoreline should not create spurious effects near the target depth (<1000 m), based on the adjustment length approach presented by Ranganayaki and Madden (1980). The selection of measurement stations along the profiles was based on the establishment of a rectangular grid. This grid was designed to facilitate the observation of transitions between profiles while minimizing potential interference from populated areas, wind turbines, or high-voltage power lines. Therefore, the obtained grid deviates slightly from the design, although the station locations are generally acceptable to allow comparison between profiles. However, MT station 22 on profile-2 (Figure 1) was an exception because the location was too noisy due to nearby wind turbines and underground

high-voltage power lines. Therefore, the data from this station were not used for modeling.

Data acquisition and instrumentation

The measurements were conducted using a Metronix ADU-07e receiver unit, manufactured in Braunschweig, Germany. This receiver unit is equipped with a high-quality 24-bit analog-to-digital converter. It is directly connected to the EFP-06 electric field probes and the MFS-07 induction coil sensors. Sampling rates of 65536 Hz, 16384 Hz, 4096 Hz, 1024 Hz, 512 Hz, and 128 Hz were used to record electromagnetic time series for durations of 2 min, 4 min, 8 min, 16 min, 32 min, and 1440 min, respectively, equal to 24 h at each MT station. The electric field electrodes, sealed with lead chloride, were buried at least 0.5 m deep and spaced approximately 100 m apart to avoid external distortions during the measurements.

Because the response of an induction coil is governed by the rate of change of magnetic flux, which is directly proportional to the time derivative of the magnetic field (Simpson and Bahr, 2005), a broadband induction coil was used to measure the magnetic field component by exploiting its high sensitivity to rapidly changing fields. Figure 3 shows the time series data obtained from station 12, one of the 32 stations included in the study (refer to Figure 1). The uniqueness of this record lies in its inclusion of the signature of the Mw = 4.2 Edremit Bay earthquake, which occurred at 08:12:47 (UTM) on 16 September 2017.

Method of calculating the impedance tensors and phase angles

Before commencing the PSO procedure, it is necessary to compute the impedance tensor to acquire the phase angles for a total of 32 stations. The software package *ProcMT* (Friedrichs, 2015) of the Metronix, which can be used to perform most of the data processing steps, was used to obtain the apparent resistivities and phase angles from the impedance tensors. The spectral ratios of the electric and magnetic fields were obtained by repeatedly applying the fast Fourier transform to a portion of the data set selected from a time window. We removed the bias effect, which mainly affects the amplitude of the transfer function, using the remote reference

method defined by Gamble et al. (1979) to obtain a robust estimation of the impedance tensor after the data processing steps.

After all these data processing steps are completed, the impedance tensor (Z), which defines the relationship between the electric field (E) and the magnetic field (H), can be expressed as follows (Simpson and Bahr, 2005):

$$\begin{bmatrix} E_x \\ E_y \end{bmatrix} = \begin{bmatrix} Z_{xx} & Z_{xy} \\ Z_{yx} & Z_{yy} \end{bmatrix} \begin{bmatrix} H_x \\ H_y \end{bmatrix} \tag{1}$$

Berdichevsky et al., (1989) propose effective impedance tensor (Z_{eff}) as

$$Z_{\text{eff}} = \sqrt{Z_{xx} \cdot Z_{yy} - Z_{xy} \cdot Z_{yx}} \tag{2}$$

and the phase angles can be calculated using equation 2 as

$$\phi_{(\omega)} = \tan^{-1} \left(\frac{Z_{\text{eff}} \text{im}(\omega)}{Z_{\text{eff}} \text{re}(Z(\omega))} \right) \tag{3}$$

where ω is the angular frequency, ϕ is the phase angle, and Z_{eff} is the effective impedance tensor in equation 2. As a good way to delineate the structural changes, and reproduce the response of the model for comparison, we preferred to use phase angles in equation 3, which are generally not affected by galvanic distortion (Jones, 1988), similar to the phase tensor presented by Caldwell et al. (2004) and Rung-Arunwan et al. (2022). The recursion formula in Wait (1954), based on the 1D MT forward model, was used to construct the forward model for PSO.

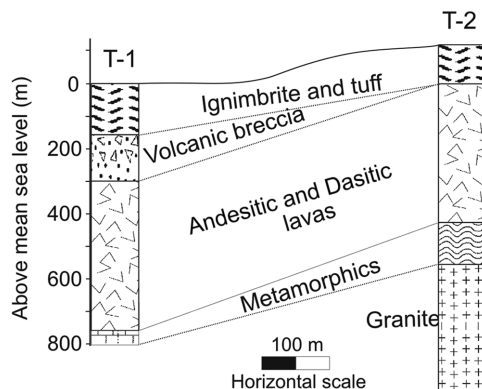


Figure 2. Geologic cross section constructed from borehole logs of T-1 and T-2 in Akkuş et al. (2005). The long-term reaction of andesitic-dacitic lavas with thermal fluid is responsible for the formation of the hydrothermal alteration zone.

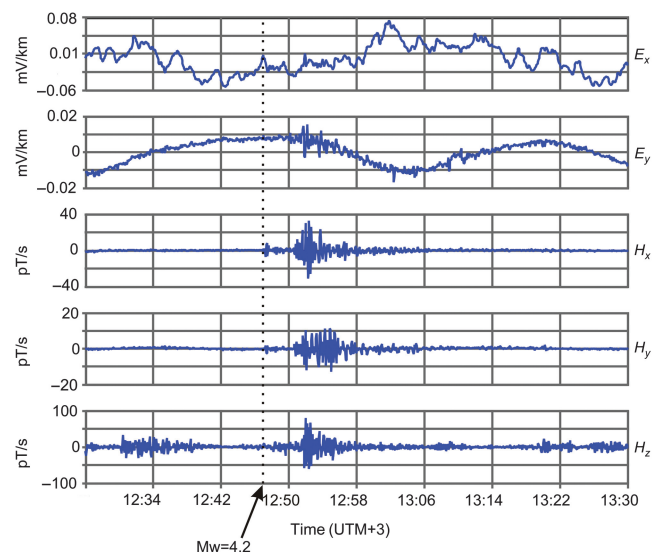


Figure 3. An example of the time series obtained at station 12. The record contains coincidentally the signature of an earthquake with Mw = 4.2, which occurred at a distance of approximately 25 km. The components of $E_{x,y}$ are the x- and y-components of the electrical field, and $H_{x,y,z}$ are the magnetic field components.

PARTICLE SWARM OPTIMIZATION

PSO, introduced by Kennedy and Eberhart (1995), is a stochastic evolutionary global optimization technique based on the behavior of a swarm of birds or fish. Each individual in a swarm called a particle represents a potential solution with a vector \mathbf{x} of the model parameters $m = (m_1, m_2, m_3, \dots, m_p)$ in p dimensional model space and learns from the other particles so that knowledge is continuously shared within the swarm. Through this sharing, each particle changes its position with a meaningful velocity vector in objective function space and converges to a global minimum.

At the beginning, the velocities of the particles are initialized to zero, and the model parameters are randomly determined within the search space. The particle that exhibits the highest level of conformity among all the particles assessed is designated as the global leader. Subsequently, the next position is determined using the velocity vector

$$\mathbf{V}_i^{k+1} = \omega \mathbf{V}_i^k + c_1 \gamma_1 \otimes (\mathbf{x}_{pbest,i} - \mathbf{x}_i^k) + c_2 \gamma_2 \otimes (\mathbf{x}_{gbest} - \mathbf{x}_i^k), \quad (4)$$

and position vector

$$\mathbf{x}_i^{k+1} = \mathbf{x}_i^k + \mathbf{V}_i^{k+1}, \quad (5)$$

where subscript i is the particle number, superscript k is the iteration number, \mathbf{x}_i^k represents the position of the i th particle at k th iteration, \mathbf{V}_i^k represents the velocity vector of the particle, ω is the inertia weight term, c_1 and c_2 are usually referred to as “acceleration factors” (e.g., (Kennedy et al., 2001; Engelbrecht, 2007), γ_1 and γ_2 are uniformly random numbers in the range [0,1], $\mathbf{x}_{pbest,i}$ is the best position of particle i in the past, and \mathbf{x}_{gbest} is the position of the global best particle. Usually, the set of quantities [ω , c_1 , c_2] are referred to as PSO parameters in the literature.

The particles change their position with a new velocity vector \mathbf{V}_i^{k+1} , which is the vector product of \mathbf{x}_{pbest} , \mathbf{x}_{gbest} and the previously calculated velocity vector \mathbf{V}_i^k . If the updated position of a particle produces a better fit compared to the previous iteration, then the new position is updated to \mathbf{x}_{pbest} . The particle is set to \mathbf{x}_{gbest} if the updated position is the best among the other solutions. This process is repeated until the fit α becomes less than or equal to the threshold value β :

$$\alpha = \left[\frac{1}{n} \sum_{i=1}^n \frac{(\theta_i^{obs} - \theta_i^{cal})^2}{\sigma_i} \right]^{1/2} \leq \beta, \quad (6)$$

where θ_i^{obs} and θ_i^{cal} are the observed and calculated phase angles, respectively, σ_i is the standard deviation of the noise for each datum, and $i = 1 \dots n$. The implementation of the PSO algorithm in the form of a pseudocode notation as in Burden and Faires (2001) is presented in Appendix A for those who are interested in developing their own code suitable for different platforms.

Model parameterization

The PSO parameters [ω , c_1 , c_2 ,] were chosen as [0.729, 1.494, 1.494] as presented by Clerc and Kennedy (2002). We constructed the earth model from four layers and used the maximum number of iterations of 100 or a threshold of 0.01 to terminate the iterations. The

number of particles was set to 70, which is 10 times the number of model parameters (four layer resistivities and three layer thicknesses), based on recent experiments on the number of particles by Pace et al. (2019). A total of 10 experimental solutions were generated multiple times, following the methodology described in the study by Pekşen et al. (2014). The final model was chosen from these solutions based on their respective fitness values, with preference given to the solution demonstrating the lowest misfit. This study uses phase angle data along with fit function in equation 6, rather than apparent resistivities that are generally affected by galvanic distortions. To achieve feasible and optimal absolute resistivities that accurately reproduce the phase angle data, it is necessary to limit the parameter search space. The parameter search space for the resistivity values in a four-layer model, as outlined in Bostick (1977), was defined as follows: the resistivity bounds for the upper layer were set to one-half and two times their original values, whereas the resistivity bounds for the lower layer were set to one-quarter and four times their original values. The layer thicknesses in the model were increased exponentially, starting at 100 m to a maximum depth given by the electromagnetic skin depth.

RESULTS AND DISCUSSION

The phase angles for two profiles and geologic cross sections from Figure 1 appear to agree, as shown in Figure 4. The dashed lines in the profiles separate the higher and lower phase angles and confirm a reasonable interface between young sediments and Balabanlı Volcanics that act as a reservoir. The structure located above the dashed lines corresponds to the Balabanlı Formation.

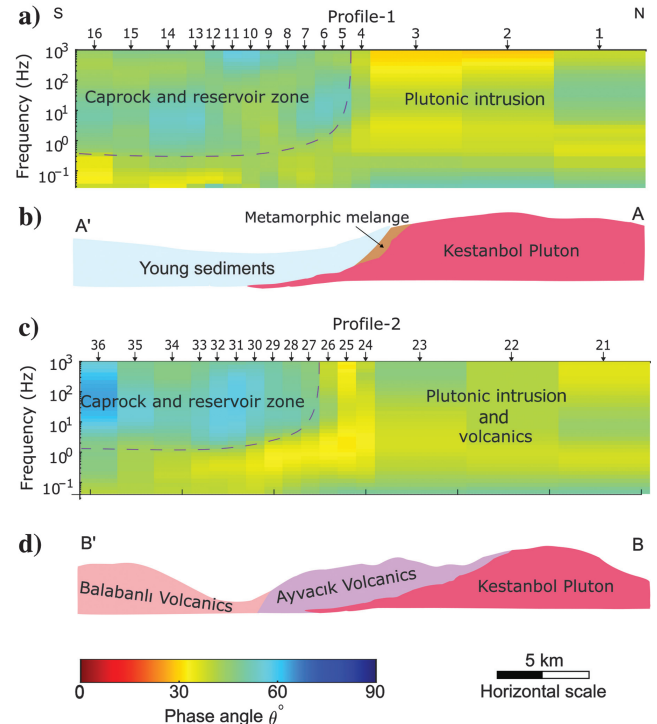


Figure 4. (a and c) Impedance phase angles and corresponding (b) geologic section along the A-A' and (d) B-B' for both profiles, respectively. The dashed line confirms a reasonable interface between the hydrothermal zone of volcanics and the metamorphic basement, mimicking the geologic interfaces in (b and d).

It exhibits relatively high phase angles, which indicates low resistivity. This behavior is commonly observed in caprock structures and reservoir zones. The presence of a relatively low phase angle below the dashed line suggests the possibility of plutonic intrusion into the metamorphic basement.

The results of the dimensionality analysis obtained from the impedance tensors, some of which are shown in Figure 5, clearly indicate a 1D structure in high-frequency ranges, as we have considered in this project, as opposed to multidimensional structures in low-frequency ranges. The image in the figure was produced at each frequency from stations 4 to 16 in Profile-1 and from stations 24 to 36 in Profile-2 using the skew values described by Swift (1967) and the dimensionless parameters of Simpson and Bahr (2005, p. 83). The result of this analysis is that the boundary at approximately 1 Hz in Figure 5 clearly mimics the interface between low and high phase angles, marked as a dashed line in Figure 4. The results obtained from the profiles indicate that the caprock and reservoir zones, which are characterized by high-frequency regions, can be effectively addressed as a 1D problem instead of a multidimensional one. Hence, our attention was directed toward the data within the frequency range below 1 Hz, commonly referred to as the audio-MT range. This particular frequency range is less susceptible to the complexities associated with higher dimensionality. Our objective was to derive an optimal and viable solution for an exploration depth of approximately 1.5 km.

Figure 6 depicts a segment of the resistivity cross sections, specifically from stations 4 to 16 in Profile-1 (Figure 6a) and from stations 24 to 36 in Profile-2 (Figure 6b). The images were constructed from the four-layered resistivity-depth models obtained by inversion of the 1D phase angles using PSO. The number of layers was limited to achieve a well-constrained and meaningful geologic model. This decision was made because excessive parameterization, when combined with data that lacks sufficient resolving power, can result in a model

outcome that is potentially unrealistic and/or influenced by inaccurately resolved model parameters (Constable et al., 1987). Therefore, using such a model outcome to make a geologic interpretation is difficult. Figure 6 shows a magnified view of the possible reservoir and caprock beneath the stations previously indicated as the focus of this work. The region denoted as Zone C in the resistivity cross sections exhibits characteristics of a caprock structure, featuring a central failed zone that is visible at a minimum of two stations. The depth of the layer identified as andesitic and dacitic volcanics, as deduced from the T1 and T2 borehole logs (refer to Figure 2), exhibits apparent coincidence in the resistivity cross sections.

The dominance of illite and mixed-layer illite-smectite clay minerals at the site as an indication of increasing clay content appears to be strong evidence for the existence and coarse form of the caprock consisting of andesitic and dacitic volcanics. Although andesitic and dacitic volcanics generally have high resistivity values, a small increase in clay content can drastically drop the resistivity values to approximately 1–5 ohm.m (Stanley et al., 1977). A contour gap of 5 ohm.m above the zone labeled M in the resistivity cross sections in Figure 6, labeled as *caprock failure*, consistently exhibits a horizontal discontinuity that may be attributed to various factors, such as a change in pressure or water chemistry following the hydrothermal mixing after the caprock failure. The presence of this zone provides confirmation of the documented temperature decreases and alterations in water chemistry that typically follow the combination of cold water with hydrothermal water following an earthquake. Regrettably, a pre-earthquake MT data set that could be used to distinctly identify the mixture zone with the resistivity alterations is not available to us. The zone marked R in the figure with a resistivity value higher than 30 ohm.m coincides with the Ayvacık Volcanics, whereas the resistivity of the Balabanlı Volcanics appears to be slightly lower in the south, as shown in the resistivity cross section of Profile-2 in Figure 6.

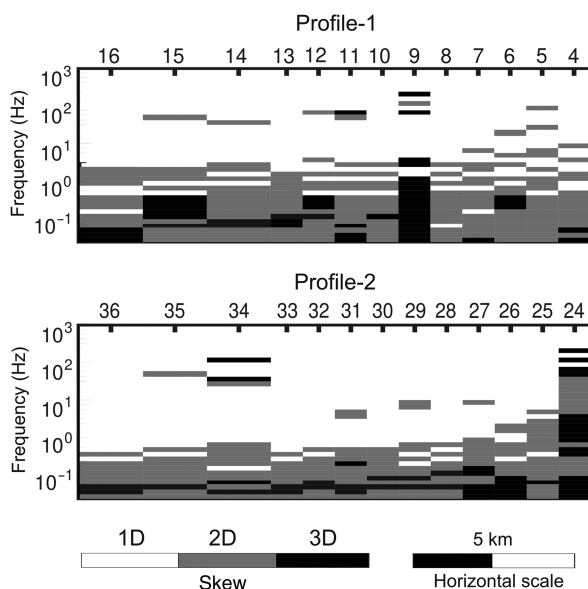


Figure 5. Magnified view of the dimensionality analysis results for (a) Profile-1 and (b) Profile-2. The numbers along the horizontal axes are the MT stations. The dominantly white zone at high-frequency ranges indicates the caprock and reservoir zones.

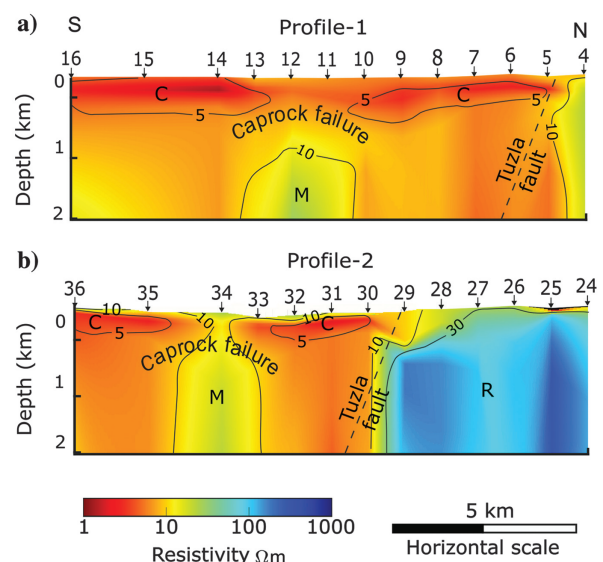


Figure 6. (a) 1D resistivity cross sections from Profile-1 and (b) Profile-2. The images were obtained using the PSO technique. The horizontal discontinuities can be considered as an indication of caprock failure related to altered pore pressure and inclusion of cold water from the overlying aquifers.

The main shock of $M_w = 5.3$ and the subsequent aftershocks, or magmatic intrusions that extend to near the surface, may be responsible for the caprock failure. Nevertheless, the existence of earthquakes that have double-couple focal mechanism solutions as shown in Figure 1 are expected to be related to the increasing effective stresses on nearby faults at some distance, as opposed to the direct product of magmatic intrusion, based on the discussion presented in Nettles and Ekström (1998). Increasing effective stress usually stabilizes a fault and also controls strain as a function of applied stress and pore pressure. Therefore, altered pore pressure resulting from the inclusion of cold water from the overlying aquifers may change the effective stress that follows the caprock failure. The induced shallow earthquakes in this case are usually characterized by low magnitudes and sometimes large periods (e.g., Freed, 2005; Steacy et al., 2005). In an alternative scenario, earthquakes can potentially be initiated through the decrease in effective normal stresses on adjacent faults subsequent to the infiltration of hydrothermal fluid into fractures, thereby elevating pressure at shallower depths. This phenomenon bears resemblance to the model that has been put forth by Martens and White (2013).

Many studies suggest that magmatic-hydrothermal eruptions are triggered by earthquakes and that these events are sometimes mutually dependent on large-scale tectonic motions (e.g., Siebert, 1984; Linde and Sacks, 1998; Feuillet et al., 2011). The magmatism-related hydrothermal activities that develop as a result of these events lead to crustal inflation by the intrusion of magma and crustal deflation by the ejection of magmatic volatiles (Bartel et al., 2003). Although presented data and models do not have sufficient resolution to find a magma reservoir in the deeper part of the hydrothermal zone, the relatively high-resistive zone labeled M is possibly related to the gas phase of the hydrothermal water filling the pores in the rock or to temperature differences of the clay mineral due to the inclusion of cold water from the overlying aquifers, as indicated by Yamaya et al. (2013).

The observed and estimated phase angles and their differences are shown in Figure 7 for Profile-1 and Profile-2. The phase angle images in the figure have been magnified to show only the portion that was shown in Figure 6. The phase angle calculations are clearly comparable with the observed phase angles, with a maximum residual of less than 10° for the profiles. These images show us that we were able to successfully identify the complex structure of the damaged caprock using the PSO modeling approach.

Phase angle and apparent resistivity data sets of three selected stations from the profiles are presented in Figure 8 for further discussion of the solution. The phase angle data along with the 1D resistivity-depth solution and model phase angles are presented in Figure 8a and 8b. The PSO solution is acceptable because the model phase angles as indicated with red lines remain within the standard deviation. The solution for station 12 is slightly resistive, whereas the layer thicknesses are nearly identical compared with the solutions for stations 6 and 16. The obtained resistivity-depth functions demonstrate a reciprocal relationship between layer thickness and resistivity. These functions accurately depict the lateral discontinuity, specifically the zone labeled C in Figure 6, without any indication of modeling artifacts. However, the Profile-2 resistivity-depth functions, shown in Figure 8b, exhibit similar characteristics (i.e., layer thicknesses) compared with the model in Figure 8a. In addition, visual inspection of the data sets from stations 6 and 16 compared with station 12 and stations 31 and 36 compared with

station 34 also emphasizes a distinct lateral discontinuity in the model. Therefore, the zone encircled with 5 ohm.m contour, marked as Zone C above Zone M, can be attributed to caprock failure and subsequent hydrothermal mixing. Reproduced and observed apparent resistivities of the selected stations are shown in Figure 8c and 8d. Although apparent resistivity data were not used to obtain a 1D model in this study, reproducing the apparent resistivities obtained from a 1D model may be an indication that the phase angle data alone can be reliable to obtain a satisfying model if the parameter search space is well constrained. The alignment between the observed apparent resistivity data and the model's predicted outcomes appears to be reasonably accurate and satisfactory.

Figures 9 and 10 show a posteriori probability density function (PDF) of the estimated parameters with mean and standard deviation from the solutions of stations 6 and 31 as examples. A posteriori PDFs contain useful information to quantify the uncertainties for each model parameter, which appear to be uniquely resolvable. A lengthy discussion of the standard deviations is not necessary because the estimated parameters have similar orders of magnitude and are within similar acceptable ranges.

This modeling approach appears to provide a methodology for MT modeling without the difficulties compared with the other global optimization methods or derivative-based inversion techniques. The PDFs of the parameters estimated by PSO in Figures 9 and 10 show a unique global model without an initial model dependency and a solution that is not trapped in a local minima, as is usually the case with conventional inversion techniques. However, PSO, similar to other global optimization techniques, also is very computationally intensive. Because our objective was limited with optimizing only a few parameters, the average computation time for each MT station's data was approximately 20 s on a 4-core

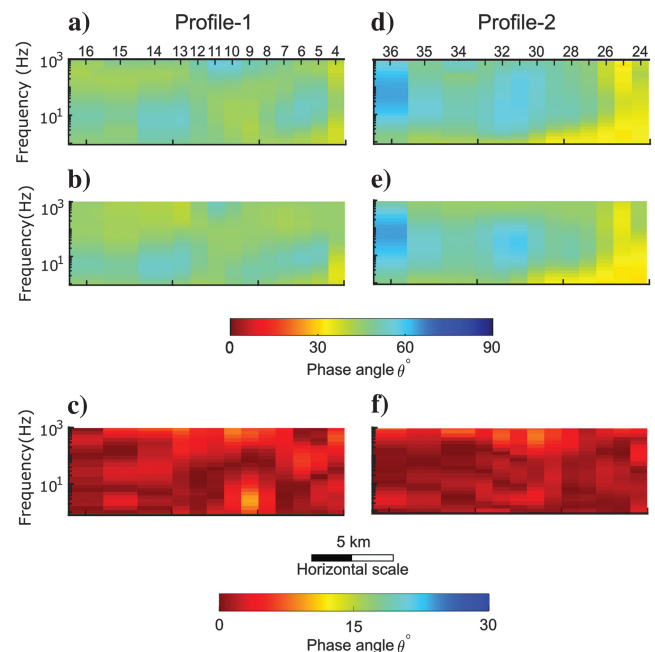


Figure 7. (a and d) The observed and (b and e) calculated impedance phase angles, and (c and f) the absolute differences, respectively. The data interpretations and the modeling approach can be assumed valid and successful given the similarities between the observed and calculated phase angles.

Figure 8. Phase angles selected from three stations and their respective 1D resistivity-depth models for (a) Profile-1 and (b) Profile-2. Reproduced phase angles appear to be reasonably close to the observed phase angles. Our modeling approach appears to successfully reproduce the apparent resistivities obtained from three stations for (c) Profile-1 and (d) Profile-2. The final model having the lowest fit was selected after 10 experimental solutions.

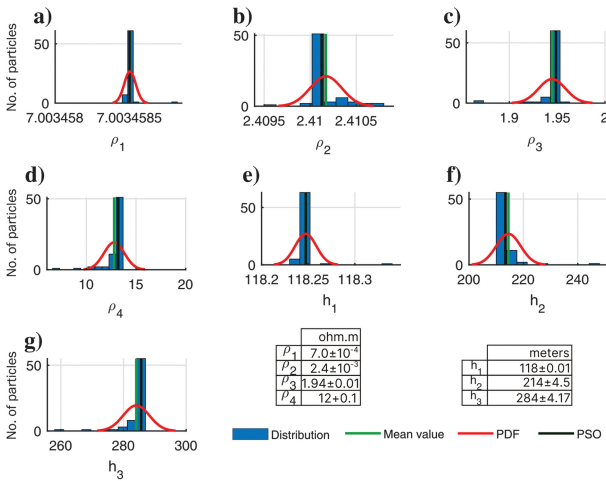
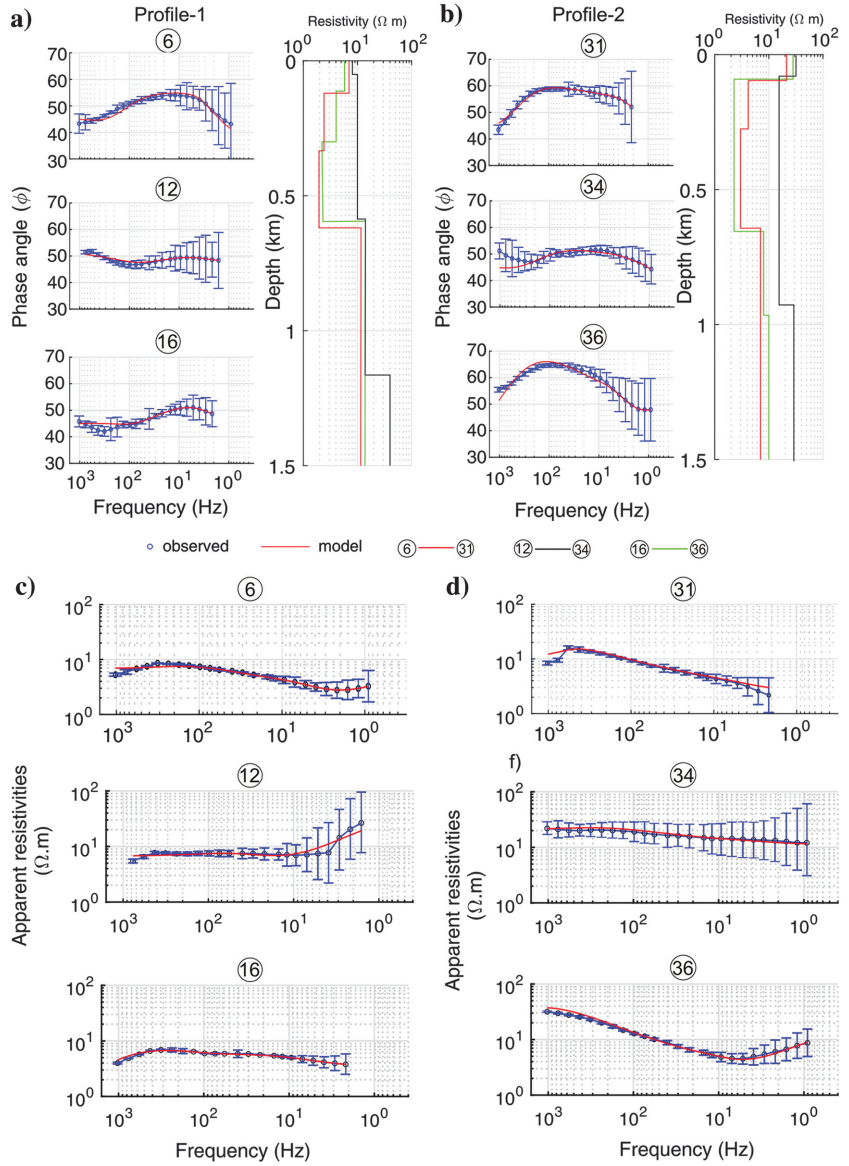


Figure 9. Posterior PDF of the estimated parameters with mean and standard deviation, with reference to interpretation at station 6.

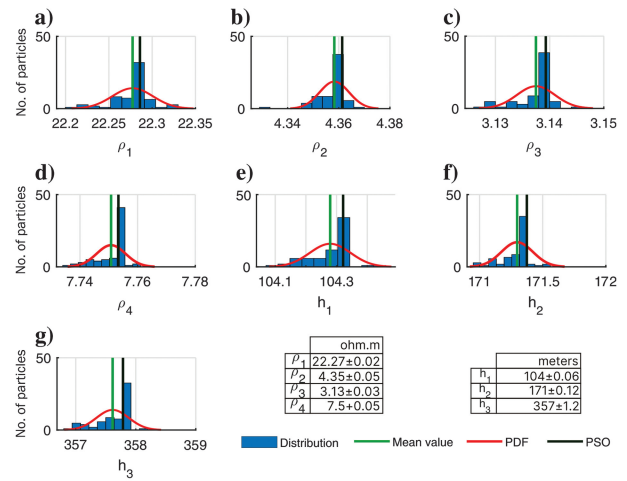


Figure 10. Posterior PDF of the estimated parameters with mean and standard deviation, with reference to interpretation at station 31.

node of a central processing unit model, i.e., a 3rd Gen Intel Core i7, 2.40 GHz with 8 GB RAM. However, a good way to avoid the time-consuming computations in the case of a high number of parameters and thus the number of particles is to parallelize the PSO code on a high-performance cluster (Pace et al., 2019).

CONCLUSION

This study used MT data processed and modeled using the PSO technique to assess the caprock integrity of the Çanakkale-Tuzla geothermal field. The data acquisition process was conducted at a total of 32 stations, spanning two profiles, in the immediate aftermath of a seismic event of moderate magnitude. Several significant conclusions can be derived from this study. (1) The observations and modeling methodology used in this study effectively ascertained the condition of the caprock. Although the occurrence of caprock failure is observable, the underlying mechanism responsible for this failure remains speculative but may be clarified through modeling using additional alternative data sets. (2) This is the initial instance in which we have approached the issue of caprock integrity at this particular location. Unfortunately, we lack a preearthquake MT data set or time-lapse measurements to clearly substantiate our interpretations. However, our results appear to reflect a hydrothermal mixture zone delineated with a low resistivity contour as occurs after pore pressure change that leads to inclusion of cold water from the overlying aquifer. Therefore, preearthquake MT data may not be vital to inspect the postearthquake status of the caprock, provided that temperature and geochemistry data are available at nearby geothermal fields. (3) This study has the potential to increase researchers' awareness of the importance of acquiring additional evidence through monitoring programs, such as temperature or geochemical surveys. These programs can enhance our comprehension of the challenges associated with caprock integrity in areas where it is anticipated to be problematic. This study also may provide a basis for sealing capacity tests in the future to assess geothermal sustainability after an earthquake with an epicenter near a geothermal field. This study also may provide a basis for modeling geothermal fields for adverse effects after excess exploitation or secondary porosity increase after an earthquake for reservoir modeling. (4) The integration of images derived from PSO can serve as a foundation for modeling reservoir temperature by representing reservoir resistivity and geometry. The application of the PSO modeling technique to MT data offers a robust methodology that avoids the generation of initial model-dependent solutions, which is a common limitation of conventional inversion techniques.

ACKNOWLEDGMENTS

This project was supported by TÜBİTAK-MAM Earth Science Research Group, Istanbul Technical University (ITU) Coordinatorship of Scientific Research Project (BAP), and The Council of Higher Education (YÖK). We thank Ü. Aşar from ITU, M. C. Tapırdamaz, and A. Arslan from TÜBİTAK-MAM Earth Science Research Group for their support in the field work to acquisition of the magnetotelluric data. We would like to extend our sincere thanks to B. Fryer and two anonymous reviewers for their critical comments and suggestions.

DATA AND MATERIALS AVAILABILITY

Data associated with this research are confidential and cannot be released.

APPENDIX A

PSEUDOCODE OF THE PSO

Figure A-1 outlines the implementation of the PSO algorithm.

```

1  for each particle (i) in an swarm
2  Set [ $x_{min} < \bar{x}_i < x_{max}$ ]
3  Set  $\vec{V}_i = 0$ 
4  Set  $\bar{x}_i = \bar{x}_{pbest,i}$ 
5  end for
6  while  $\alpha \geq \beta$ 
7  for  $i = 1 \dots n$  (number of particle)
8  Evaluate an objective function  $f(x_i)$ 
9  if  $f(x_i) < f(x_{pbest,i})$ 
10  Set  $\bar{x}_i$  to  $\bar{x}_{pbest,i}$ 
11  end if
12  end for
13  Set  $\bar{x}_{pbest,i}$  having best fit value as the  $g_{best}$ 
14  for each particle (i) in an swarm
15  Update  $\vec{V}_i$  using Eq. (4)
16  Update  $\bar{x}_i$  using Eq. (5)
17  end for
18  end while

```

Figure A-1. Implementation of PSO algorithm for a minimization problem.

REFERENCES

- Akal, C., 2013, Coeval Shoshonitic-ultrapotassic dyke emplacements within the Kestanol Pluton, Ezine-Biga Peninsula (NW Anatolia): Turkish Journal of Earth Sciences, **22**, 220–238, doi: [10.3906/yer-1202-1](https://doi.org/10.3906/yer-1202-1).
- Akkuş, İ., H. Akıllı, S. Ceyhan, A. Dilemre, and Z. Tekin, 2005, MTA Genel Müdürlüğü Yayınları, Envanter Serisi-201: Ankara.
- Aldanmaz, E., J. A. Pearce, M. F. Thirlwall, and J. G. Mitchell, 2000, Petrogenetic evolution of late Cenozoic, post-collision volcanism in western Anatolia, Turkey: Journal of Volcanology and Geothermal Research, **102**, 67–95, doi: [10.1016/S0377-0273\(00\)00182-7](https://doi.org/10.1016/S0377-0273(00)00182-7).
- Altunkaynak, Ş., Y. Dilek, C. Genç, G. Sunal, R. Gertisser, H. Furnes, K. A. Foland, and J. Yang, 2012, Spatial, temporal and geochemical evolution of Oligo-Miocene granitoid magmatism in western Anatolia, Turkey: Gondwana Research, **21**, 961–986, doi: [10.1016/j.gr.2011.10.010](https://doi.org/10.1016/j.gr.2011.10.010).
- Altunkaynak, Ş., and C. Genç, 2008, Petrogenesis and time-progressive evolution of the Cenozoic continental volcanism in the Biga Peninsula, NW Anatolia (Turkey): Lithos, **102**, 316–340, doi: [10.1016/j.lithos.2007.06.003](https://doi.org/10.1016/j.lithos.2007.06.003).
- Aslan, Z., D. Erdem, İ. Temizel, and M. Arslan, 2017, SHRIMP U–Pb zircon ages and whole-rock geochemistry for the Şapçı volcanic rocks, Biga Peninsula, Northwest Turkey: Implications for pre-eruption crystallization conditions and source characteristics: International Geology Review, **59**, 1764–1785, doi: [10.1080/00206814.2017.1295282](https://doi.org/10.1080/00206814.2017.1295282).
- Baba, A., M. M. Demir, G. A. Koç, and C. Tuğcu, 2015, Hydrogeological properties of hyper-saline geothermal brine and application of inhibiting siliceous scale via pH modification: Geothermics, **53**, 406–412, doi: [10.1016/j.geothermics.2014.08.007](https://doi.org/10.1016/j.geothermics.2014.08.007).
- Bartel, B. A., M. W. Hamburger, C. M. Meertens, A. R. Lowry, and E. Cor-puz, 2003, Dynamics of active magmatic and hydrothermal systems at Taal Volcano, Philippines, from continuous GPS measurements: Journal of Geophysical Research: Solid Earth, **108**, 2475, doi: [10.1029/2002JB002194](https://doi.org/10.1029/2002JB002194).
- Beccaletto, L., 2003, Geology, correlations, and geodynamic evolution of the geology, correlations, and geodynamic evolution of the Biga Peninsula (NW Turkey): PhD Dissertation, Université de Lausanne.
- Berdichevsky, M. N., L. L. Vanyan, and V. I. Dmitriev, 1989, Methods used in the U.S.S.R. to reduce near-surface inhomogeneity effects on deep magnetotelluric sounding: Physics of the Earth and Planetary Interiors, **53**, 194–206, doi: [10.1016/0031-9201\(89\)90003-4](https://doi.org/10.1016/0031-9201(89)90003-4).

- Bonabeau, E., D. Marco, and T. Guy, 1999, Swarm intelligence: From natural to artificial systems: Santa Fe Institute Studies in the Sciences of Complexity, Oxford University Press.
- Bostick, F., 1977, A simple almost exact method of MT analysis: Workshop on Electrical Methods in Geothermal Exploration, University of Utah, 175–177.
- Bozkaya, Ö., G. Bozkaya, I. T. Uysal, and D. A. Banks, 2016, Illite occurrences related to volcanic-hosted hydrothermal mineralization in the Biga Peninsula, NW Turkey: Implications for the age and origin of fluids: *Ore Geology Reviews*, **76**, 35–51, doi: [10.1016/j.oregeorev.2016.01.001](https://doi.org/10.1016/j.oregeorev.2016.01.001).
- Burden, R. L., and D. Faires, 2001, Numerical analysis, 7th ed.: Thomson Learning, Inc.
- Buyuk, E., E. Zor, and A. Karaman, 2017, Rayleigh wave dispersion curve inversion by using particle swarm optimization and genetic algorithm: 19th EGU General Assembly, 6911.
- Caldwell, T. G., H. M. Bibby, and C. Brown, 2004, The magnetotelluric phase tensor: *Geophysical Journal International*, **158**, 457–469, doi: [10.1111/j.1365-246X.2004.02281.x](https://doi.org/10.1111/j.1365-246X.2004.02281.x).
- Clerc, M., and J. Kennedy, 2002, The particle swarm-explosion, stability, and convergence in a multidimensional complex space: *IEEE Transactions on Evolutionary Computation*, **6**, 58–73, doi: [10.1109/4235.985692](https://doi.org/10.1109/4235.985692).
- Constable, S. C., R. L. Parker, and C. G. Constable, 1987, Occam's inversion: A practical algorithm for generating smooth models from electromagnetic sounding data: *Geophysics*, **52**, 289–300, doi: [10.1190/1.1442303](https://doi.org/10.1190/1.1442303).
- Cui, Y., L. Zhang, X. Zhu, J. Liu, and Z. Guo, 2020, Inversion for magnetotelluric data using the particle swarm optimization and regularized least squares: *Journal of Applied Geophysics*, **181**, 104156, doi: [10.1016/j.jappgeo.2020.104156](https://doi.org/10.1016/j.jappgeo.2020.104156).
- Cumming, W., and R. Mackie, 2010, Resistivity imaging of geothermal resources using 1D, 2D and 3D MT inversion and TDEM static shift correction illustrated by a Glass Mountain case history: Proceedings World Geothermal Congress, 1–10.
- Dewey, J. F., and A. M. C. Şengör, 1979, Aegean and surrounding regions: Complex multiplate and continuum tectonics in a convergent zone: *Bulletin of the Geological Society of America*, **90**, 84–92, doi: [10.1130/0016-7606\(1979\)90<84:AASRCM>2.0.CO;2](https://doi.org/10.1130/0016-7606(1979)90<84:AASRCM>2.0.CO;2).
- Eberhart, R. C., and Y. Shi, 1998, Comparison between genetic algorithms and particle swarm optimization: International Conference on Evolutionary Programming, 611–616.
- Emre, Ö., and A. Doğan, 2010, 1/250.000 Ölçekli Türkiye Diri Fay Haritaları Serisi: Ayvalık (NJ 35-2) Paftası, Seri No:2.
- Engelbrecht, A. P., 2007, Computational intelligence: An introduction, 2nd ed.: John Wiley & Sons, Ltd.
- Fernández Martínez, J. L., E. García Gonzalo, J. P. Fernández Álvarez, H. A. Kuzma, and C. O. Menéndez Pérez, 2010, PSO: A powerful algorithm to solve geophysical inverse problems: Application to a 1D-DC resistivity case: *Journal of Applied Geophysics*, **71**, 13–25, doi: [10.1016/j.jappgeo.2010.02.001](https://doi.org/10.1016/j.jappgeo.2010.02.001).
- Feuillet, N., F. Beauducel, E. Jacques, P. Tapponnier, B. Delouis, S. Bazin, M. Vallée, and G. C. P. King, 2011, The Mw = 6.3, November 21, 2004, les Saintes earthquake (Guadeloupe): Tectonic setting, slip model and static stress changes: *Journal of Geophysical Research: Solid Earth*, **116**, 1–25.
- Freed, A. M., 2005, Earthquake triggering by static, dynamic, and postseismic stress transfer: Annual Review of Earth and Planetary Sciences, **33**, 335–367, doi: [10.1146/annurev.earth.33.092203.122505](https://doi.org/10.1146/annurev.earth.33.092203.122505).
- Friedrichs, B., 2015, ProcMT online manual, https://www.geo-metronix.de/procmt_html/, accessed 24 October 2018.
- Fytikas, M., O. Giuliani, F. Innocenti, G. Marinelli, and R. Mazzuoli, 1976, Geochronological data on recent magmatism of the Aegean Sea: *Tectonophysics*, **31**, T29–T34, doi: [10.1016/0040-1951\(76\)90161-X](https://doi.org/10.1016/0040-1951(76)90161-X).
- Gamble, T., W. Goubau, and J. Clarke, 1979, Error analysis for remote reference magnetotellurics: *Geophysics*, **44**, 959–968, doi: [10.1190/1.1440988](https://doi.org/10.1190/1.1440988).
- Gill, M. K., Y. H. Kaheil, A. Khalil, M. McKee, and L. Bastidas, 2006, Multi-objective particle swarm optimization for parameter estimation in hydrology: *Water Resources Research*, **42**, 1–14, doi: [10.1029/2005WR004528](https://doi.org/10.1029/2005WR004528).
- Godio, A., and A. Santilano, 2018, On the optimization of electromagnetic geophysical data: Application of the PSO algorithm: *Journal of Applied Geophysics*, **148**, 163–174, doi: [10.1016/j.jappgeo.2017.11.016](https://doi.org/10.1016/j.jappgeo.2017.11.016).
- Hassan, R., B. Cohanım, O. De Weck, and G. Venter, 2005, A comparison of particle swarm optimization and the genetic algorithm: AIAA/ASME/ASCE/AHS/ASC Structures, Structural Dynamics and Materials Conference, 1138–1150.
- Iguchi, M., 2013, Magma movement from the deep to shallow Sakurajima Volcano as revealed by geophysical observations: *Bulletin of the Volcanological Society of Japan*, **58**, 1–18, doi: [10.18940/kazan.58.1_1](https://doi.org/10.18940/kazan.58.1_1).
- Jones, A. G., 1988, Static shift of magnetotelluric data and its removal in a sedimentary basin environment: *Geophysics*, **53**, 967–978, doi: [10.1190/1.1442533](https://doi.org/10.1190/1.1442533).
- Jones, A. G., and I. Dumas, 1993, Electromagnetic images of a volcanic zone: *Physics of the Earth and Planetary Interiors*, **81**, 289–314, doi: [10.1016/0031-9201\(93\)90137-X](https://doi.org/10.1016/0031-9201(93)90137-X).
- Kaplanvural, İ., E. Pekşen, and K. Özkap, 2020, 1D waveform inversion of GPR trace by particle swarm optimization: *Journal of Applied Geophysics*, **181**, 104157, doi: [10.1016/j.jappgeo.2020.104157](https://doi.org/10.1016/j.jappgeo.2020.104157).
- Karacık, Z., and Y. Yılmaz, 1998, Geology of the Ignimbrites and the associated volcano-plutonic complex of The Ezine: *Journal of Volcanology and Geothermal Research*, **85**, 251–264, doi: [10.1016/S0377-0273\(98\)00058-4](https://doi.org/10.1016/S0377-0273(98)00058-4).
- Karcioglu, G., and A. Güner, 2019, Implementation and model uniqueness of particle swarm optimization method with a 2D smooth modeling approach for radio-magnetotelluric data: *Journal of Applied Geophysics*, **169**, 37–48, doi: [10.1016/j.jappgeo.2019.06.001](https://doi.org/10.1016/j.jappgeo.2019.06.001).
- Kennedy, J., and R. Eberhart, 1995, Particle swarm optimization: IEEE International Conference on Neural Networks, 1942–1948.
- Kennedy, J., and R. C. Eberhart, 2002, Swarm intelligence: *IEEE Technology and Society Magazine*, **21**, 9–10, doi: [10.1007/0-387-27705-6_6](https://doi.org/10.1007/0-387-27705-6_6).
- Kennedy, J., and W. M. Spears, 1998, Matching algorithms to problems: An experimental test of the particle swarm and some genetic algorithms on the multimodal problem generator: Proceedings of the IEEE Conference on Evolutionary Computation, 78–83.
- Kennedy, J. F., R. C. Eberhart, and Y. Shi, 2001, Swarm intelligence: Morgan Kaufmann Publishers.
- Li, M., J. Cheng, P. Wang, Y. Xiao, W. Yao, C. Su, S. Cheng, J. Guo, and X. Yu, 2019, Transient electromagnetic 1D inversion based on the PSO–DLS combination algorithm: *Exploration Geophysics*, **50**, 472–480, doi: [10.1080/08123985.2019.1627172](https://doi.org/10.1080/08123985.2019.1627172).
- Lichoro, C. M., K. Arnason, and W. Cumming, 2017, Resistivity imaging of geothermal resources in northern Kenya rift by joint 1D inversion of MT and TEM data: *Geothermics*, **68**, 20–32, doi: [10.1016/j.geothermics.2017.02.006](https://doi.org/10.1016/j.geothermics.2017.02.006).
- Linde, A. T., and I. S. Sacks, 1998, Triggering of volcanic eruptions: *Nature*, **395**, 888–890.
- Maffucci, R., S. Corrado, L. Aldega, S. Bigi, A. Chiodi, L. Di Paolo, G. Giordano, and C. Invernizzi, 2016, Cap rock efficiency of geothermal systems in fold-and-thrust belts: Evidence from paleo-thermal and structural analyses in Rosario de La Frontera geothermal area (NW Argentina): *Journal of Volcanology and Geothermal Research*, **328**, 84–95, doi: [10.1016/j.jvolgeores.2016.10.008](https://doi.org/10.1016/j.jvolgeores.2016.10.008).
- Mannen, K., Y. Abe, Y. Daita, R. Doko, M. Harada, G. Kikugawa, N. Honma, Y. Miyashita, and Y. Yukutake, 2021, Volcanic unrest at Hakone volcano after the 2015 phreatic eruption: Reactivation of a ruptured hydrothermal system? *Earth, Planets and Space*, **73**, 1–15, doi: [10.1186/s40623-021-01387-3](https://doi.org/10.1186/s40623-021-01387-3).
- Martens, H. R., and R. S. White, 2013, Triggering of microearthquakes in Iceland by volatiles released from a dyke intrusion: *Geophysical Journal International*, **194**, 1738–1754, doi: [10.1093/gji/ggt184](https://doi.org/10.1093/gji/ggt184).
- McKenzie, D., 1978, Active tectonics of the Alpine — Himalayan belt: The Aegean Sea and surrounding regions: *Geophysical Journal of the Royal Astronomical Society*, **55**, 217–254, doi: [10.1111/j.1365-246X.1978.tb04759.x](https://doi.org/10.1111/j.1365-246X.1978.tb04759.x).
- Muñoz, G., 2014, Exploring for geothermal resources with electromagnetic methods: *Surveys in Geophysics*, **35**, 101–122, doi: [10.1007/s10712-013-9236-0](https://doi.org/10.1007/s10712-013-9236-0).
- Mutzenberg, S., 1997, Nature and origin of the thermal springs in the Tuzla Area, Western Anatolia, Turkey, in C. Schindler and M. Pfister, eds., Active tectonic of Northwestern Anatolia — The Marmara Poly-Project: VDF Hochschul Verlag AG an der ETH Zurich, 301–317.
- Nettles, M., and G. Ekström, 1998, Faulting mechanism of anomalous earthquakes near Bárðarbunga Volcano, Iceland: *Journal of Geophysical Research: Solid Earth*, **103**, 17973–17983, doi: [10.1029/98JB01392](https://doi.org/10.1029/98JB01392).
- Okay, A. I., M. Satir, H. Maluski, M. Siyako, P. Monie, R. Metzger, and S. Akyüz, 1996, Paleo- and Neo-Tethyan events in northwest Turkey: Geological and geochronological constraints, in A. Yin and M. Harrison, eds., The tectonic evolution of Asia: Cambridge University Press, 420–441.
- Olalekan, F., and Q. Di, 2017, Particle swarm optimization method for 1D and 2D MTEM data inversion: 87th Annual International Meeting, SEG, Expanded Abstracts, 1219–1224, doi: [10.1190/segam2017-17671977.1](https://doi.org/10.1190/segam2017-17671977.1).
- Özden, S., S. Över, S. A. Poyraz, Y. Güneş, and A. Pınar, 2018, Tectonic implications of the 2017 Ayvacık (Çanakakke) earthquakes, Biga Peninsula, NW Turkey: *Journal of Asian Earth Sciences*, **154**, 125–141, doi: [10.1016/j.jseaes.2017.12.021](https://doi.org/10.1016/j.jseaes.2017.12.021).
- Pace, F., A. Santilano, and A. Godio, 2019, Particle swarm optimization of 2D magnetotelluric data: *Geophysics*, **84**, no. 3, E125–E141, doi: [10.1190/geo2018-0166.1](https://doi.org/10.1190/geo2018-0166.1).
- Pace, F., A. Santilano, and A. Godio, 2021, A review of geophysical modeling based on particle swarm optimization: *Surveys in Geophysics*, **42**, 505–549, doi: [10.1007/s10712-021-09638-4](https://doi.org/10.1007/s10712-021-09638-4).
- Pallero, J. L. G., J. L. Fernandez-Martinez, S. Bonvalot, and O. Fudym, 2015, Gravity inversion and uncertainty assessment of basement relief via particle swarm optimization: *Journal of Applied Geophysics*, **116**, 180–191, doi: [10.1016/j.jappgeo.2015.03.008](https://doi.org/10.1016/j.jappgeo.2015.03.008).

- Pekşen, E., T. Yas, and A. Kiyak, 2014, 1-D DC resistivity modeling and interpretation in anisotropic media using particle swarm optimization: *Pure and Applied Geophysics*, **171**, 2371–2389, doi: [10.1007/s00024-014-0802-2](https://doi.org/10.1007/s00024-014-0802-2).
- Ranganayaki, R. P., and T. R. Madden, 1980, Generalized thin sheet analysis in magnetotellurics: An extension of Price's analysis: *Geophysical Journal of the Royal Astronomical Society*, **60**, 445–457, doi: [10.1111/j.1365-246X.1980.tb04820.x](https://doi.org/10.1111/j.1365-246X.1980.tb04820.x).
- Rung-Arunwan, T., W. Siripunvaraporn, and H. Utada, 2022, The effect of initial and prior models on phase tensor inversion of distorted magnetotelluric data: *Earth, Planets and Space*, **74**, 1–24, doi: [10.1186/s40623-022-01611-8](https://doi.org/10.1186/s40623-022-01611-8).
- Samrock, F., A. Kuvshinov, J. Bakker, A. Jackson, and S. Fisseha, 2015, 3-D analysis and interpretation of magnetotelluric data from the Aluto-Langano geothermal field, Ethiopia: *Geophysical Journal International*, **202**, 1923–1948, doi: [10.1093/gji/ggv270](https://doi.org/10.1093/gji/ggv270).
- Şanlıyüksel Yücel, D., S. Özden, and H. Marmara, 2021, Hydrogeochemical and isotopic monitoring of the Kestanbol geothermal field (Northwestern Turkey) and its relationship with seismic activity: *Turkish Journal of Earth Sciences*, **30**, 1112–1133, doi: [10.3906/yer-2105-15](https://doi.org/10.3906/yer-2105-15).
- Şener, M., and A. I. Gevrek, 2000, Distribution and significance of hydrothermal alteration minerals, Çanakkale, Turkey: *Journal of Volcanology and Geothermal Research*, **96**, 215–228, doi: [10.1016/S0377-0273\(99\)00152-3](https://doi.org/10.1016/S0377-0273(99)00152-3).
- Shaw, R., and S. Srivastava, 2007, Particle swarm optimization: A new tool to invert geophysical data: *Geophysics*, **72**, no. 2, F75–F83, doi: [10.1190/1.2432481](https://doi.org/10.1190/1.2432481).
- Siebert, L., 1984, Large volcanic debris avalanches: Characteristics of source areas, deposits, and associated eruptions: *Journal of Volcanology and Geothermal Research*, **22**, 163–197, doi: [10.1016/0377-0273\(84\)90002-7](https://doi.org/10.1016/0377-0273(84)90002-7).
- Simpson, F., and K. Bahr, 2005, *Practical magnetotellurics*: Cambridge University Press, 272.
- Song, J., and D. Zhang, 2013, Comprehensive review of caprock-sealing mechanisms for geologic carbon sequestration: *Environmental Science and Technology*, **47**, 9–22, doi: [10.1021/es301610p](https://doi.org/10.1021/es301610p).
- Stanley, W. D., J. E. Boehl, F. X. Bostick, and H. W. Smith, 1977, Geothermal significance of magnetotelluric sounding in the Eastern Snake River Plain-Yellowstone region: *Journal of Geophysical Research*, **82**, 2501–2514, doi: [10.1029/JB082i017p02501](https://doi.org/10.1029/JB082i017p02501).
- Steady, S., J. Gombert, and M. Cocco, 2005, Introduction to special section: Stress transfer, earthquake triggering, and time-dependent seismic hazard: *Journal of Geophysical Research: Solid Earth*, **110**, 1–12, doi: [10.1029/2005JB003692](https://doi.org/10.1029/2005JB003692).
- Swift, C. M., 1967, A magnetotelluric investigation of an electrical conductivity anomaly in the South Western United States: Ph.D. Thesis, M.I.T., Cambridge, Mass.
- Taymaz, T., J. Jackson, and D. McKenzie, 1991, Active tectonics of the north and central Aegean Sea: *Geophysical Journal International*, **106**, 433–490, doi: [10.1111/j.1365-246X.1991.tb03906.x](https://doi.org/10.1111/j.1365-246X.1991.tb03906.x).
- Ussher, G., C. Harvey, R. Johnstone, E. Anderson, and N. Zealand, 2000, Understanding the resistivities observed in geothermal systems: *Proceedings World Geothermal Congress*, 1915–1920.
- Wait, J. R., 1954, On the relation between telluric currents and the earth's magnetic field: *Geophysics*, **19**, 281–289, doi: [10.1190/1.1437994](https://doi.org/10.1190/1.1437994).
- Yalçın, H. T., 1989, Çanakkale-Tuzla Kaplıcası dolayının hidrojeolojisi ve kaynağının kökeninin araştırılması: Yüksek Lisans Tezi, İTÜ Fen Bilimleri Enstitüsü.
- Yamaya, Y., P. K. B. Alanis, A. Takeuchi, J. M. Cordon, T. Mogi, T. Hashimoto, Y. Sasai, and T. Nagao, 2013, A large hydrothermal reservoir beneath Taal Volcano (Philippines) revealed by magnetotelluric resistivity survey: 2D resistivity modeling: *Bulletin of Volcanology*, **75**, 1–13, doi: [10.1007/s00445-013-0729-y](https://doi.org/10.1007/s00445-013-0729-y).
- Yılmaz, Y., 1990, Comparison of young volcanic associations of western and eastern Anatolia formed under a compressional regime: A review: *Journal of Volcanology and Geothermal Research*, **44**, 69–87, doi: [10.1016/0377-0273\(90\)90012-5](https://doi.org/10.1016/0377-0273(90)90012-5).
- Yılmaz, Y., C. Genç, Z. Karacık, and Ş. Altunkaynak, 2001, Two contrasting magmatic associations of NW Anatolia and their tectonic significance: *Journal of Geodynamics*, **31**, 243–271, doi: [10.1016/S0264-3707\(01\)00002-3](https://doi.org/10.1016/S0264-3707(01)00002-3).
- Yuan, S., S. Wang, and N. Tian, 2009, Swarm intelligence optimization and its application in geophysical data inversion: *Applied Geophysics*, **6**, 166–174, doi: [10.1007/s11770-009-0018-x](https://doi.org/10.1007/s11770-009-0018-x).

Biographies and photographs of the authors are not available.